ARTICLE

Check for updates

High-resolution stalagmite stratigraphy supports the Late Holocene tephrochronology of southernmost Patagonia

Björn Klaes [1,2 ✉], Gerhard Wörner [3], Katrina Kremer[4], Klaus Simon[3], Andreas Kronz [5], Denis Scholz [6], Carsten W. Mueller [7], Carmen Höschen [8], Julian Struck [9], Helge Wolfgang Arz [10], Sören Thiele-Bruhn[2], Daniel Schimpf[1] & Rolf Kilian[1,11,12]

Volcanic ash layers are important markers for the chronostratigraphy of paleoclimate and paleoenvironmental archives at the southern tip of South America. However, this requires that tephras are well-dated. We report geochemical data from stalagmite MA1 formed in a non-karst cave near Mt. Burney volcano in southernmost Patagonia (~53°S). High-resolution LA-ICP-MS analyses, SEM imagery, EPMA data, and NanoSIMS enable to identify volcano-genic signals during the last 4.5 kyrs from sub-annual trace element variations and tephra particles in distinct laminae. Our new ^{230}Th/U-chronology of MA1 provides precise dating of tephra from Mt. Burney (MB) and, probably, Aguilera (A) at 4,216 $^{+93}/_{-193}$ yrs BP (MB$_2$), 2,291 ± 33 yrs BP (MB$_3$), 853 $^{+41}/_{-60}$ yrs BP (MB$_4$) and 2,978 $^{+91}/_{-104}$ yrs BP (A$_1$). This unique high-resolution record holds potential to date further eruptions from Southern Andean volcanoes for the tephrochronology in this critical region, and potentially also large-volume explosive volcanism off South America.

[1] Geology Department, Trier University, Campus II (Geozentrum), Behringstraße 21, 54296 Trier, Germany. [2] Soil Science Department, Trier University, Campus II (Geozentrum), Behringstraße 21, 54296 Trier, Germany. [3] Division of Geochemistry and Isotope Geology, GZG, Georg-August-University Göttingen, Goldschmidtstraße 1, 37077 Göttingen, Germany. [4] Swiss Seismological Service, ETH Zürich, Sonneggstrasse 5, 8092 Zürich, Switzerland. [5] Department of Mineralogy, GZG, Georg-August-University Göttingen, Goldschmidtstraße 1, 37077 Göttingen, Germany. [6] Institute for Geosciences, Johannes Gutenberg University Mainz, Johann-Joachim-Becher-Weg 21, 55128 Mainz, Germany. [7] Department for Geosciences and Environmental Management, University of Copenhagen, Øster Voldgade 10, 1350 København K, Denmark. [8] Soil Science, Research Department Life Science Systems, TUM School of Life Sciences, Technical University of Munich, Emil-Ramann-Straße 2, 85354 Freising-Weihenstephan, Germany. [9] Department of Physical Geography, Institute of Geography, Friedrich-Schiller-University Jena, Löbdergraben 32, 07743 Jena, Germany. [10] Marine Geology Department, Leibniz Institute for Baltic Sea Research Warnemünde (IOW), Seestraße 15, 18119 Rostock, Germany. [11] University of Magallanes, Avenida Bulnes, 01855 Punta Arenas, Chile. [12] Deceased: Rolf Kilian. ✉email: klaesb@uni-trier.de

Severe and long-lasting impact on regional ecosystems from explosive volcanic eruptions and ash (tephra) fallout has been observed in fragile environments such as the super-humid South Patagonian Andes[1,2]. While geochemical fingerprinting links tephra glass shard compositions to their volcanic source and represents a valuable tool in tephrochronology[3], the dating of distinct tephra layers enables a reconstruction of the regional history of volcanic activity and provides isochronous and stratigraphic marker horizons for the correlation of paleoenvironmental archives over large geographical areas[4]. Despite intensive research and rapid advances in the development of tephrochronological methods in the past few decades, the accurate identification of distinct tephra layers and the precise synchronization of single volcanic events recorded in geological archives from different depositional environments remains challenging[4,5].

In southernmost Patagonia, the ages of widespread Holocene tephra layers from Plinian eruptions from volcanoes of the Patagonian Andes[6] in the southern segment of the Southern (41.5–46°S) and the Austral (49–55°S) Volcanic Zones were mainly deduced from ^{14}C-dated materials of terrestrial outcrops, peat and marine/lacustrine sediment cores[3,5,7,8]. This tephrochronological framework constitutes the principal reference for the stratigraphy of most geological records used in paleoclimate/paleoenvironmental studies from this climatically unique and poorly explored region[9].

But accurate age constraints for sedimentary climate and environmental archives are particularly difficult to obtain because age uncertainties and problems with the correlation of tephra layers in regional soils and sediment or peat core archives are due to variable composition, unclear stratigraphy, and diverging chronologies based on ^{14}C-dated carbonates, bulk organic matter (OM) or single plant remains[3,4]. In particular, ^{14}C-dated components of soils and sediments can have age offsets of hundreds of years due to reservoir effects caused by, e.g., the re-sedimentation and bioturbation of older OM or carbonate dissolution[10,11], which have serious implications for age models. Large errors in age determination of volcanic ash layers also occur from the interpolation of bracketing ^{14}C dates[4] and/or age constraints based on estimated sedimentation/peat accumulation rates[12,13].

Further challenges include the correct identification of the source volcano through the characteristic physical/textural properties as well as the mineralogical and geochemical composition of tephra pumice and glass shards[8]. Site-dependent, potentially intense weathering processes in acidic peatland ecosystems[14] can compromise geochemical fingerprinting methods for tephra correlation[3]. Chemical weathering over long periods strongly alters the composition of volcanic glass and embedded phenocrysts, leading to changes in the concentration of major and trace elements[15–17].

Despite their increasingly important role as high-resolution terrestrial archives for the reconstruction of past climate and environmental changes, only a few speleothem records have so far contributed to regional tephrochronologies worldwide[18–22]. This is due to the difficulty of detecting unequivocal volcanic signals in speleothems. Furthermore, speleothem layers containing tephra glass shards or even small pumice particles have — to our knowledge — not yet been documented. Paine et al.[23], for example, emphasized that the site-specific hydrological regime and soil/vegetation perturbation may attenuate the chemical signals from explosive volcanism that are preserved in stalagmites. Moreover, chemical signals of volcanic ash deposition can outlast the actual eruptive events by millennia[1]. These effects contribute to complicate the identification of volcanic eruptions by the sole stalagmite trace element profiling.

Nevertheless, speleothems can be very useful for such studies because [230]Th/U dating allows exceptionally accurate and precise dating and variations in chemical elements can be detected with up to (sub-) annual resolution. Therefore, speleothems have great potential for the high precision dating of volcanic events comparable to ice core tephra records[18,24]. Combined with stable isotope data ($\delta^{18}O$, $\delta^{13}C$) and trace element proxies, speleothem records enable both the dating of volcanic activity and the evaluation of possible environmental and climate impacts following the documented eruptions[18–21].

In this work, we analyze a non-karst speleothem (stalagmite MA1[25]) to better constrain the Late Holocene tephrostratigraphy in southernmost Patagonia and provide evidence for soil–environmental changes related to tephra deposition under extreme climate conditions. This speleothem formed in a small cave ca. 40 km S of Mt. Burney volcano and recorded sub-annual trace element variations detected by laser ablation inductively coupled plasma mass spectrometry (LA-ICP-MS). These high-resolution compositional profiles were combined with a refined [230]Th/U-chronology age model constructed from published[25] and additional new [230]Th/U dates. Based on this improved age model, our new LA-ICP-MS data, and principal component analysis (PCA), we (i) detect and analyze pyroclastic particles incorporated into the stalagmite and (ii) correlate these particles to pristine tephra of Mt. Burney volcano by electron microprobe (EPMA) glass composition measurements. This allows (iii) to precisely date the MB_2, MB_3, and MB_4 tephra using the improved age model for the speleothem archive based on [230]Th/U-ages. Furthermore, (iv) the MA1 record documents the environmental response to changes in the hydrological/pedological regime caused by the eruptions and their deposits. We also identify a chemical signal of the A_1 eruption of Aguilera and provide a new age estimate for this eruption as well. In addition, (v) EPMA measurements, scanning electron microscopy (SEM), and nanoscale secondary ion mass spectrometry (NanoSIMS) of detrital components preserved in distinct laminae confirm the identification of pristine and reworked tephra particles and their alteration products. Within the context of the data reported here, previously published stable isotope data ($\delta^{18}O$, $\delta^{13}C$) of MA1[25] provide additional constraints on short-term perturbations of the local surface hydrology and soil composition following the eruptions.

Environmental context and characteristics of stalagmite MA1. The MA1 stalagmite was obtained from the Marcelo Arévalo (MA) cave[25], situated at 20 m a.s.l. in the Magellanic moorlands at 52°41.50′S/73°16.28′W (Fig. 1a). The cave formed in a nearly vertical tectonic fracture zone cross-cutting a plutonic sequence of coarse-crystalline granite with mylonitic orthogneiss and rare mafic dykes[26]. Granite and orthogneiss mainly comprise quartz, plagioclase, and mica. The most prominent accessory minerals are pyrite, apatite, and zircon. Rarely occurring mafic intrusives are mainly composed of hornblende, plagioclase, clinopyroxene, and a few mica. Accessory phases include, e.g., apatite and zircon. The hydrological system in this fracture zone directly connects the cave with a small catchment (~2500 m²) at 80 m a.s.l. that is characterized by acidic (pH 3.9–5.7), waterlogged peatland soils, and surrounding bare rock outcrops[26] (Fig. 1b). The super-humid climate in this region is controlled by pronounced seasonal variations of the southern westerly wind belt[27–29] (SWW), present annual precipitation of ~3800 mm yr^{-1}[30], and mean annual temperatures of 5.3 °C[30] (recorded at the automatic weather station Arévalo; Fig. 1c). Reconstructed annual precipitation during the Late Holocene reached up to 6500 mm yr^{-1}[25]. Monitoring data between 2005 and 2008 reveal that cave temperatures
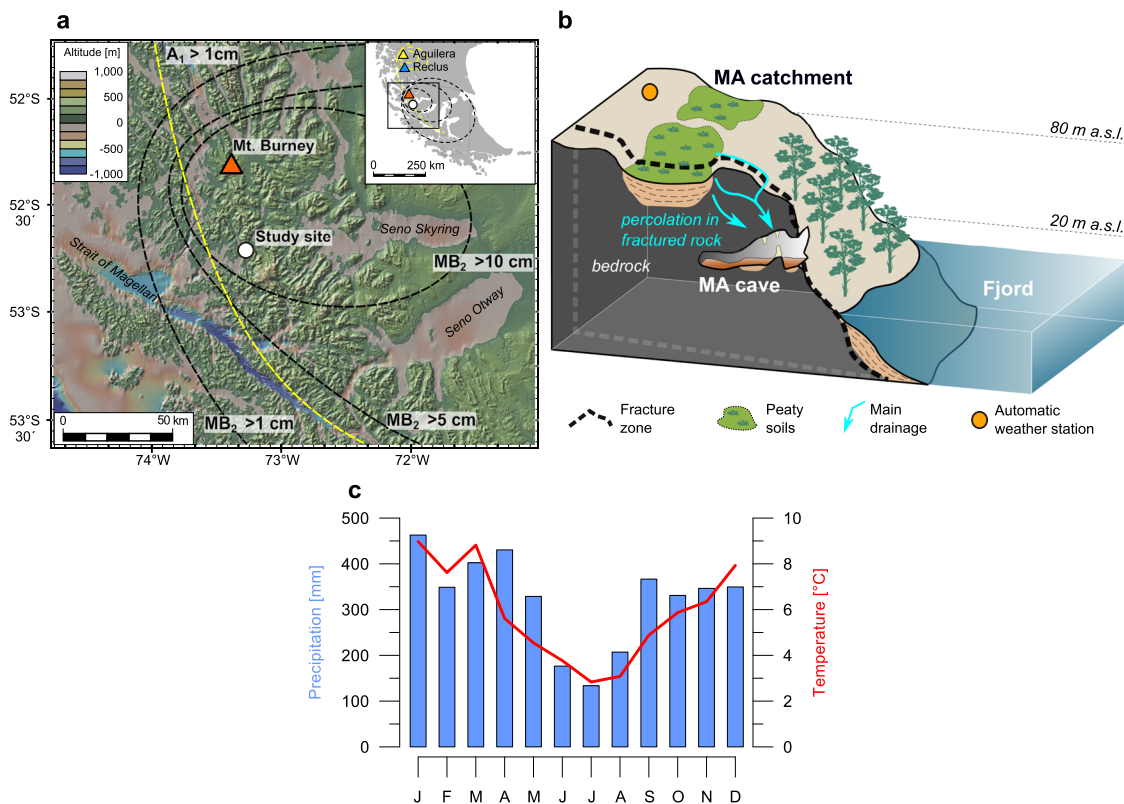
Fig. 1 Location of the study area and site characteristics. a The study site at the windward side of the southernmost Andes, ~40 km S of the Mt. Burney volcano. Inserted isopach lines indicate the thickness and distribution of tephra deposits from the MB$_2$ and A$_1$ eruption[7]. In addition, Reclus and Aguilera volcanoes are shown. **b** Marcelo Arévalo[25] (MA) cave and its environmental context. The hydrological connection between the cave and its catchment is schematically illustrated. **c** Mean monthly precipitation and temperatures measured at the automatic weather station Arévalo[30]. Values were averaged from the time spans 2011–2012 and 2015–2016. The background map in **a** was generated with GeoMapApp[77,78].

do not differ from atmospheric values and that average relative humidity is 94%[25]. The drip water has a pH of 7.5 and elevated average drip rates (~150–250 cm^3 d^{-1}) measured at the MA1 sampling site vary within the seasonal trend[25]. An estimated maximum delay of only 4–6 weeks between major rainfall events and related drip rate increase[25] indicates a relatively high transmissivity of the fractured aquifer system due to good connectivity of the cave with the local surface hydrology in combination with the extraordinary precipitation. Stalagmite MA1 shows a rather constant mean growth rate of 67 μm yr^{-1} (minor variations of 25–100 μm yr^{-1})[25] and continuous growth over the last 4.5 kyrs BP (before present, year 1950 of the common era). A significant hiatus, interrupting the growth of MA1, has not been observed[25]. Along the growth axis, MA1 is dominated by compact calcite, whereas marginal areas and distinct sections rich in OM and detrital silicate components (volcanic glass, basement-derived mineral grains; Fig. S2) are more porous. However, microscopic analyses provided no evidence for CaCO$_3$ dissolution and/or re-crystallization[31–33] in these laminae.

The cave site is located only 40 km S of the Mt. Burney volcano (52°19′S/73°22′W, Fig. 1a), the most active volcano of the Austral Volcanic Zone during the Late Quaternary[5]. Originating from this volcano, ten Holocene Plinian eruptions dispersed tephra layers across wide areas of southernmost South America[3]. After the large-volume MB$_2$ eruption, regional pristine ecosystems suffered millennium-scale damage caused by SO$_2$-induced acidification associated with the deposition of >10 cm of volcanic ash[1,2]. By contrast, the tephra deposits from the notably smaller Mt. Burney eruptions with a volcanic explosivity index below 5[3] are only a few millimeters thick[12,13] and probably had minor

impacts on the environment. All volcanic eruptions we address in this paper are identified and named according to the database published by Fontjin et al.[3].

Results

Chronology. We used StalAge[34] to construct a new age-depth model for the MA1 speleothem compared to the previous study by Schimpf et al.[25] (Fig. 2). Our age-depth model (Table S1) is now based on 16 published and 2 new ^{230}Th/U-ages and a slightly modified detrital correction factor for Th[35]. The applied StalAge model for MA1 covers the entire 280 mm length along the growth axis of the speleothem, representing about 4.8 kyrs. For details of the ^{230}Th/U-age constraints, detritus correction, and the construction of the age model, see the "Methods" section.

Element concentrations determined by LA-ICP-MS. Concentrations of S, P, U, Si, Sr, and Zr — selected by virtue of the well-known composition of Mt. Burney tephra[7,8,36] and the environmental impact after the deposition of MB$_2$ ash[1] — were measured on multiple overlapping thin sections prepared along the entire length of MA1 (4.5–0.6 kyrs BP) and are presented in Figs. 3–5. Average elemental concentrations were determined from a total of 59,200 LA-ICP-MS measurements for S (132 ppm), P (2212 ppm), U (2.4 ppm), Si (1400 ppm), Sr (197 ppm), and Zr (3.2 ppm). Against this background, we observe numerous high amplitude spikes identified as short (few months up to three years) and strong variations in the deposition of these elements. Such peak concentrations reached >10 ppm for U and Zr, >400 ppm for Sr, >1000 ppm for S and P, and easily exceeded 10,000 ppm in the
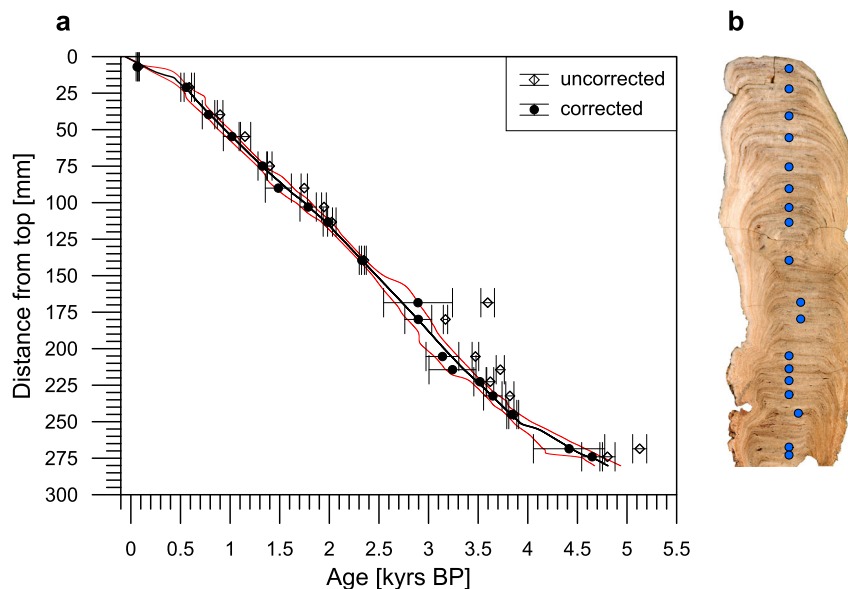
Fig. 2 New age-depth model of the MA1 stalagmite. a StalAge[34] age-depth model, including the corresponding 95% confidence limits (thin red lines). Uncorrected ages and ages after detritus correction[35] are shown with standard deviations as 2σ error bars (see Table S1 for details). **b** Photo of MA1 including the 18 sampling points for [230]Th/U dating.

case of Si (Figs. 3–5). These high amplitude spikes are well correlated for S, P, U, Si, Sr, and Zr and appear highly irregular with respect to frequency and intensity along with the profiles. Particular conspicuous spikes of S, P, U, Sr, and partly of Si and Zr, occur at 4.216, 2.978, 2.291, and 0.853 kyrs BP (orange bars; Figs. 3 and 4). These conspicuous spikes are followed by (i) a series of mostly smaller, but equally discrete, short-term peaks for the same elements decreasing in height or by (ii) more extended periods characterized by consistently elevated concentrations from ~4.20 to 4.14 kyrs BP, respectively (gray bars; Fig. 4).

As would be expected for elements that are contributed from detrital particles sourced from tephra, Si should be closely related to Zr. Indeed, Fig. 5 shows that a large number of LA-ICP-MS measurements fall on a tight correlation trend that projects from the origin with a Si/Zr ratio of 3300 toward the composition of Mt. Burney glass with average values of 77 wt.% SiO_2 and 110 ppm Zr[7,8]. A_1 glass from Aguilera has a similar Si/Zr ratio of 3600 (75.7 wt.% SiO_2 and 97 ppm Zr on average[8]), however, high Si and Zr peaks are absent in the expected section from 3.1 to 2.9 kyrs BP (Fig. 5d). By using these Si/Zr ratios, we calculated mixing lines between two endmembers: the Si- and Zr- rich Mt. Burney/Aguilera glass and the Si- and Zr-free $CaCO_3$ matrix of the speleothem (blue lines in binary plots in Fig. 5). Concentrations for Zr and Si that are higher than the concentrations in the tephra are an artifact of normalization to Ca in LA-ICP-MS measurements that include distinct but unknown amounts of a non-carbonate detrital component (i.e., basement-derived minerals, which are lower in Ca compared to $CaCO_3$). This artifact in the concentration data is unavoidable and does not affect the characteristic Si/Zr ratio of the volcanic glass mixing line. However, a large number of analyses fall off this correlation and can be attributed to silicate minerals from basement rocks. One additional component is particularly rich in Si (and low in Zr) and identifies quartz or silica gels, whereas a few data points tend towards high Zr and are likely caused by traces of detrital zircon. These minerals have also been identified on SEM micrographs.

In order to further characterize elemental peaks of Si, Zr, S, and other elements in the speleothem record and to provide for tests that these may represent volcanic signals, we analyzed the data set

using a PCA[22,37]. The first three principal components (PC) explain 80.7% of the variability within the entire data set (Figs. 6 and S1 and Table S2). High scores for PC-1 (44.4%), PC-2 (19.4%), and PC-3 (16.9%) reflect the correlated trace element peaks as discussed above and displayed in Figs. 3–5. PC-1 has high loadings of S, P, U, and Si, whereas the PC-2 loadings mirror mainly Si and Sr. Zirconium is dominantly loaded on PC-3. High PC scores, particularly of PC-1, suggest distinct depositional events at 4.216, 2.978, 2.291, and 0.853 kyrs BP. However, all PCs show high variability in score values from 4.20 to 4.15 kyrs BP and synchronous spikes during the periods 2.96–2.92, 2.27–2.17, and 0.79–0.73 kyrs BP.

Composition of detrital silicate components. Major element compositions of detrital silicate particles embedded in MA1 were analyzed by EPMA (Fig. S2 and Tables S3–S5). We detected pristine rhyolitic glass fragments in laminae at 4.21, 2.29, and 0.85 kyrs BP (78.12 wt.% SiO_2, 1.77 wt.% K_2O, 3.46 wt.% Na_2O, and 0.29 wt.% MgO on average). These compositions are identical to matrix glasses from pumice originated from Mt. Burney, but differ significantly from known compositions of other documented wide-spread tephras from Hudson and Reclus volcanoes in the Southern and Austral Volcanic Zones[5,7,8] (Fig. 3b, c). A few oscillatory zoned plagioclase and euhedral clinopyroxene crystals are also typical for Mt. Burney tephra[36] (Fig. S2c, e).

Other mineral components detected in laminae at 2.29, 1.79, 0.85, and 0.73 kyrs BP (Fig. S2 and Table S4) include ilmenite, apatite, pyroxene, biotite, plagioclase, quartz, and zircon. The occurrence of quartz at 0.76 kyrs BP is also confirmed by X-ray diffractometry, showing a peak at 3.344 Å (Fig. S2g). The composition, intergrowth textures, and shape of these mineral grains indicate that they originate from a granitic/gneissic bedrock. Additional EPMA measurements on Si-rich particles found in porous fabrics can neither be related to the composition of Mt. Burney glass nor to bedrock minerals (Table S5). These particles show a large range in composition with no relation to any mineral stoichiometry. They are, on average, significantly lower in SiO_2 (61.39 wt.%), TiO_2 (0.08 wt. % or below detection limit) Na_2O (0.50 wt.%) and K_2O (0.47 wt.%) and higher in Al_2O_3
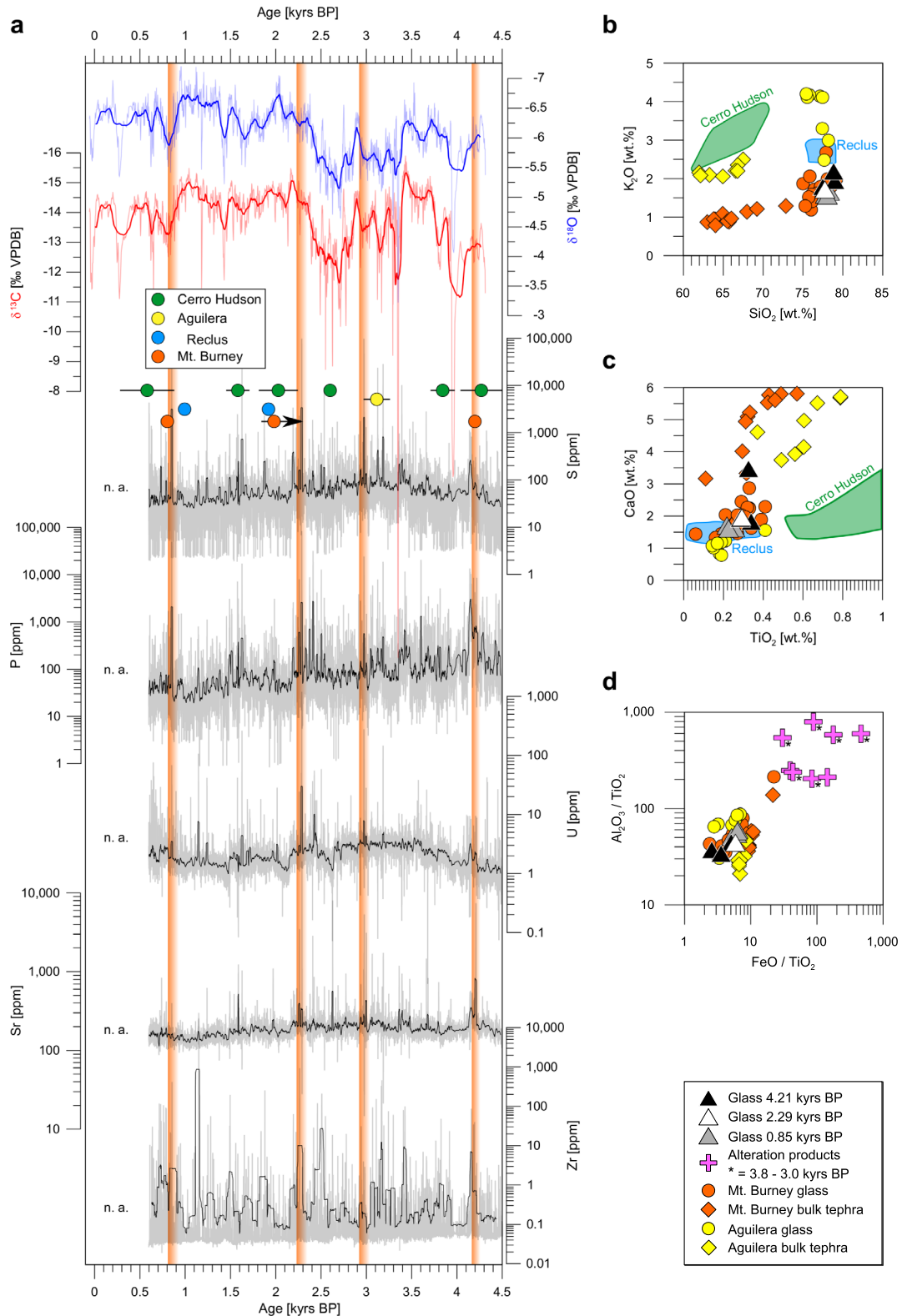
Fig. 3 Stable isotope and LA-ICP-MS data of MA1 between 4.5 and 0.6 kyrs BP combined with the geochemistry of incorporated volcanic glass and its alteration products. a $\delta^{18}O$ and $\delta^{13}C$ records[25] of the MA1 stalagmite combined with concentrations of S, P, U, Sr, and Zr. ^{14}C-ages of tephra layers from Late Holocene eruptions of volcanoes of the Southern and Austral Andean Volcanic Zone[3] are indicated. Orange bars highlight times with compositional trace element peaks at 4.216, 2.978, 2.291, and 0.853 kyrs BP. The section labeled with n.a. has not been analyzed. **b–d** EPMA analyses of volcanic glass and glass alteration products detected in MA1 together with single-glass shard and bulk tephra data from regional tephrostratigraphic marker horizons[5,7,8,13,36].
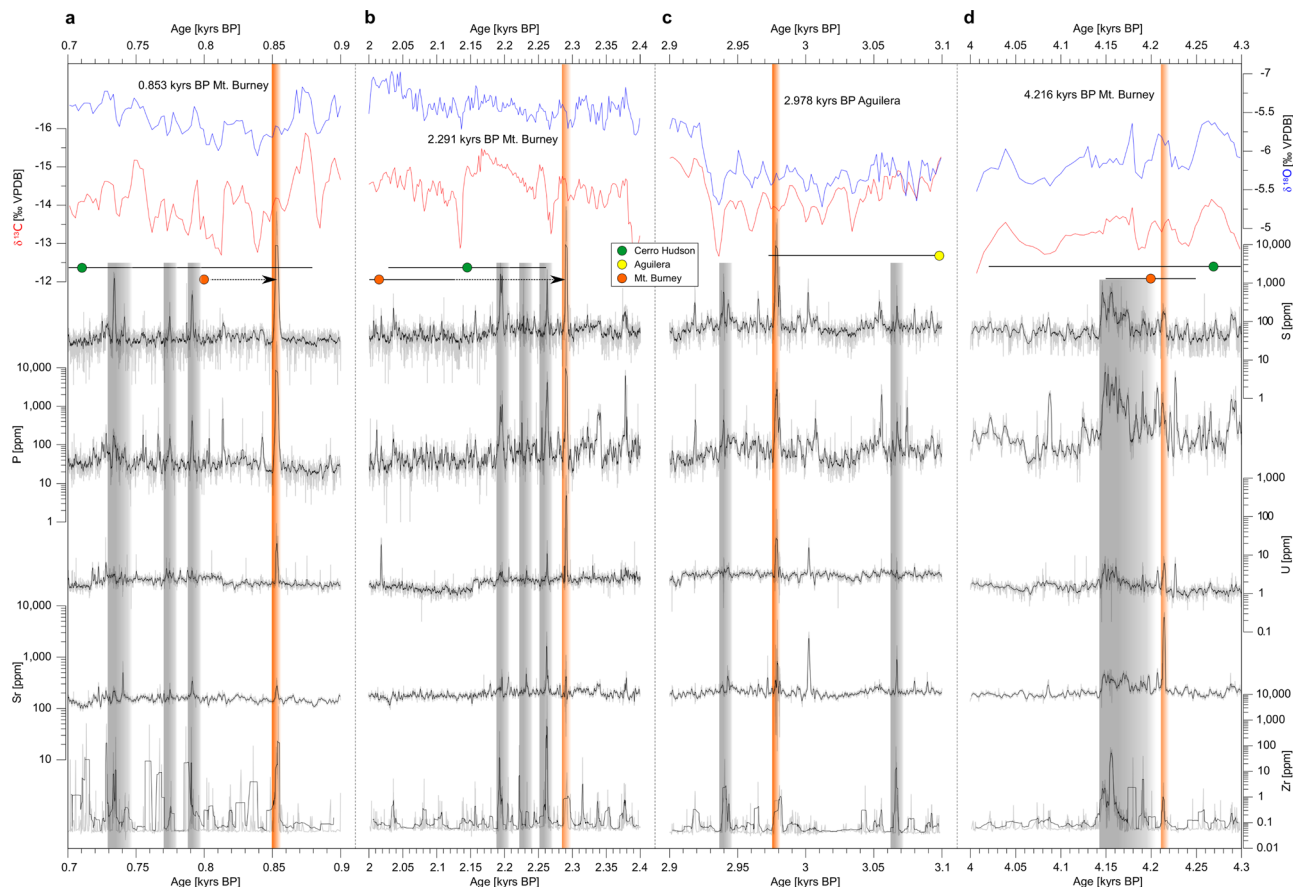
Fig. 4 Stable isotope and LA-ICP-MS data of MA1 for time spans enclosing eruptions of Mt. Burney and Aguilera volcanoes. a–d $\delta^{18}O$ and $\delta^{13}C$ records[25] of stalagmite MA1 combined with concentrations of S, P, U, Sr, and Zr (**a** 0.9–0.7 kyrs BP; **b** 2.4–2.0 kyrs BP; **c** 3.1–2.9 kyrs BP; **d** 4.3–4.0 kyrs BP). ^{14}C-ages of tephra layers from Late Holocene eruptions of Cerro Hudson, Aguilera, and Mt. Burney[3] are indicated. Orange bars highlight times with compositional trace element peaks at 4.216, 2.978, 2.291, and 0.853 kyrs BP. Gray bars mark time spans characterized by elevated incorporation of micrometer-scale detrital volcanic glass mobilized during storm events.

(24.65 wt.%), FeO (5.92 wt.%), MgO (3.73 wt.%) and CaO (3.06 wt.%) compared to glass from Mt. Burney[5,7,8]. In particular, measurements from the section between 3.8 and 3.0 kyrs BP show very high Al_2O_3/TiO_2 (>200) and FeO/TiO_2 (>30) ratios. These values strongly exceed the comparatively low Al_2O_3/TiO_2 and FeO/TiO_2 ratios of the pristine volcanic glass (47.9 and 5.1, respectively; Fig. 3d). As detailed below, we tentatively interpret these compositions as alteration products from silicate glass weathering.

Detection of tephra particles by SEM and NanoSIMS. The SEM micrographs of detrital siliciclastic components obtained after mild leaching of the $CaCO_3$ matrix of isolated laminae at 4.15 and 2.20 kyrs BP where PC scores and concentrations of Si and Zr are high are shown in Fig. 7a–c. Some layers were particularly rich in fragments of pyroclastic material, comprised of either vesicular glass shards (2.20 kyrs BP; Fig. 7a) or phenocrysts glazed with a thin coating of volcanic glass (4.15 kyrs BP; Fig. 7b, c). On thin sections, SEM micrographs reveal incorporation of a vitreous silicate component at 4.21, 2.29, and 0.85 kyrs BP (Fig. S2). These images document the preservation of tephra that was included in the growing speleothem.

Detritus-rich inclusions were further analyzed in situ by NanoSIMS (Figs. 7d–f and 8). The 30×30 μm measurement spots focused on non-carbonate materials accumulated in lamina sections at ~3.92 and ~2.29 kyrs BP. Elevated $^{28}Si^-$ and $^{16}O^-$ secondary ion counts indicate an enrichment of irregularly shaped, in part porous siliciclastic particles of 5–20 μm size with $^{12}C^-$ and $^{12}C^{14}N^-$ detected in pores (Fig. 7d–f). The particles themselves show a low incidence of $^{27}Al^{16}O^-$ counts and are framed by thin rims that are significantly enriched in $^{27}Al^{16}O^-$. The matrix surrounding these micrometer-scale particles is characterized by the spatial distribution of strong $^{12}C^-$ and $^{12}C^{14}N^-$ signals with dispersed Fe and Al as indicated by spots of $^{56}Fe^{16}O^-$ and $^{27}Al^{16}O^-$.

NanoSIMS measurements on inclusions at ~3.50 and ~3.11 kyrs BP did not detect such pristine siliciclastic particles (Fig. 8a, b). By contrast, areas with higher $^{16}O^-$, $^{28}Si^-$, $^{27}Al^{16}O^-$, and $^{56}Fe^{16}O^-$ counts appear as fine flaky structures. These structures occur scattered throughout the observed areas and correlate with high $^{12}C^-$, $^{12}C^{14}N^-$, and $^{32}S^-$ signals, here interpreted as indicative of OM. At ~0.73 kyrs BP, particles with strong localized signals of $^{28}Si^-$ and moderate $^{16}O^-$ in the absence of other measured elements (Fig. 8c) are interpreted as phenocrysts or grains of bedrock-derived mineral detritus, such as quartz (cf. identified minerals; Fig. S2 and Table S4). However, in this case, thin $^{27}Al^{16}O^-$ rims have not been observed.

Discussion
Identifying volcanic input by compositional spikes of characteristic elements in the MA1 speleothem record provides means for precise dating and the correlation of volcanic ash inputs into Patagonian soils and environmental archives[9]. In order to identify
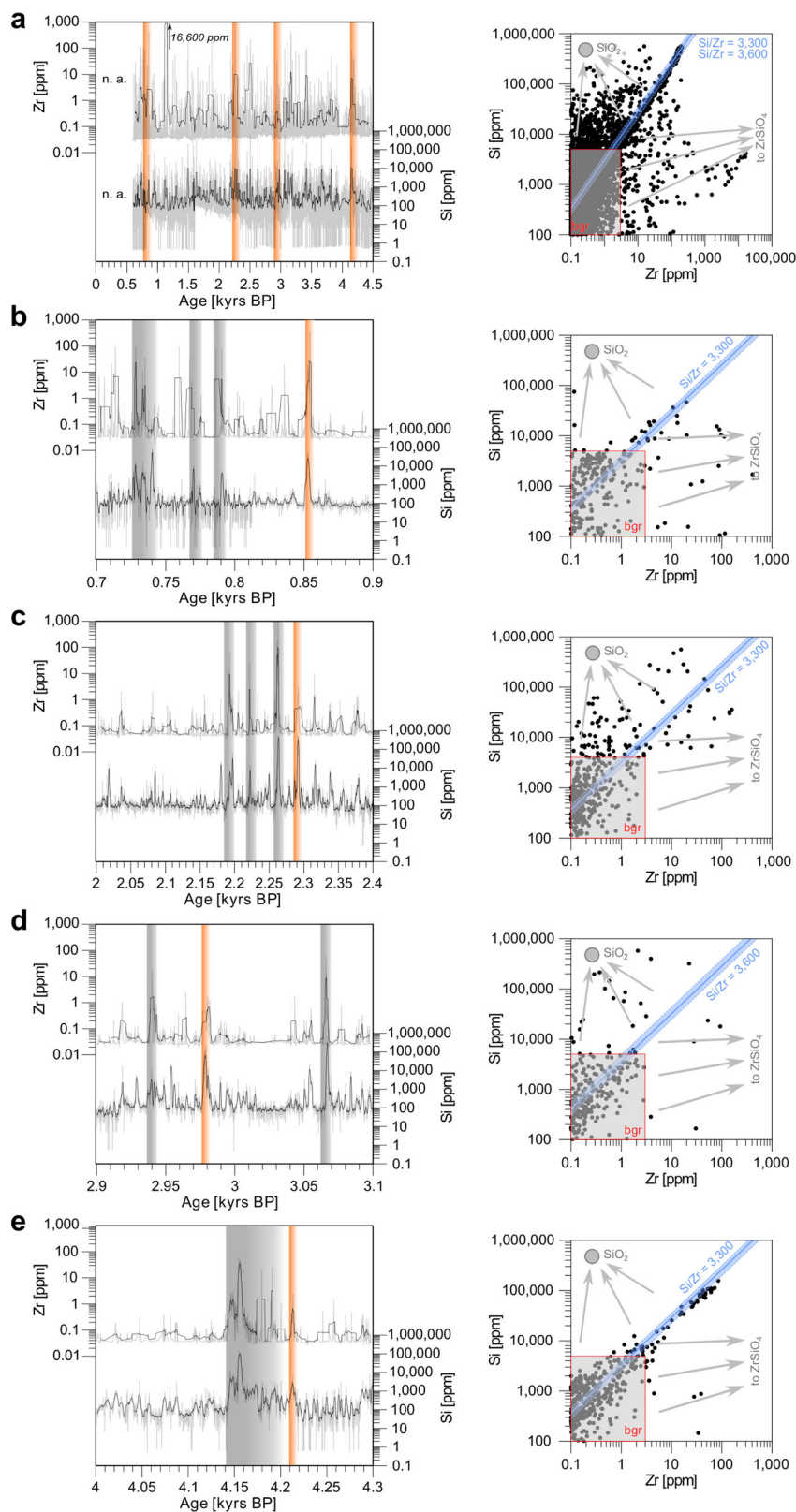
such volcanic signals, we need to consider the direct primary elemental deposition from tephra, volcanic volatiles, and leached components. In addition, there may be a secondary response to tephra deposition on peatland soils that potentially affects nutrient cycling[38], chemical leaching[15,16], and soil C stocks[39,40]. Pristine peatland ecosystems such as those of southernmost Patagonia may be particularly sensitive to volcanic impacts from

tephra-loading under extreme climate conditions[1,41]. Finally, the improved age constraints of tephra layers that we detected in MA1 allow addressing the impact that volcanic eruptions had on this super-humid environment.

There is direct evidence for tephra deposition and alteration during the growth of stalagmite MA1. The principal elemental input from tephra comes from fine-grained glassy pyroclastic

Fig. 5 Variations and relationships of Si and Zr concentrations in MA1 determined by LA-ICP-MS. a–e Si and Zr records are shown in combination with corresponding binary plots for different time spans (**a** 4.5–0.6 kyrs BP; **b** 0.9–0.7 kyrs BP; **c** 2.4–2.0 kyrs BP; **d** 3.1–2.9 kyrs BP; **e** 4.3–4.0 kyrs BP). The section labeled with n.a. has not been analyzed. Orange bars highlight times with compositional trace element peaks at 4.216, 2.978, 2.291, and 0.853 kyrs BP. Gray bars mark time spans characterized by elevated incorporation of micrometer-scale detrital volcanic glass mobilized during storm events. The binary plots indicate a correlation of LA-ICP-MS measurements on a mixing line between two endmembers: the Si- and Zr-free $CaCO_3$ and Si- and Zr-rich volcanic glass from Mt. Burney and Aguilera with Si/Zr ratios of 3300 and 3600[7,8], respectively. Vectors pointing outwards from this mixing line towards quartz and/or silica gels (SiO_2) and zircon ($ZrSiO_4$) are included. The red rectangles mark the analytical background (bgr) of the LA-ICP-MS measurements (Si <5000 ppm and Zr <3 ppm).
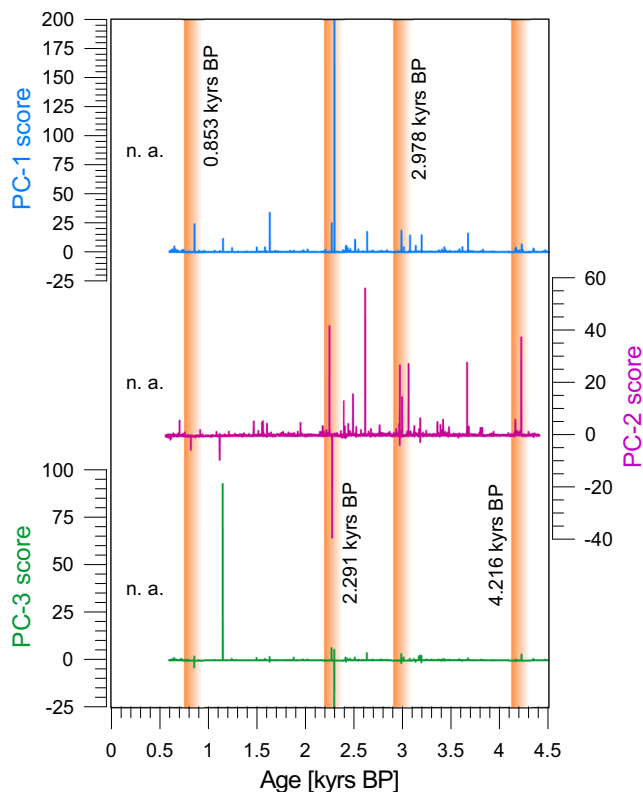
Fig. 6 Scores of the principal components PC-1, PC-2, and PC-3 performed on the LA-ICP-MS data set (S, P, U, Si, Sr, and Zr). The PCA scores of PC-1, PC-2, and PC-3 are shown for the time span from 4.5 to 0.6 kyrs BP. The section labeled with n.a. has not been analyzed. Orange bars mark periods in which the PC main spikes are synchronous with compositional trace element peaks at 4.216, 2.978, 2.291, and 0.853 kyrs BP (Figs. 3–5).

particles and is documented by synchronous and sharp peaks of Zr and Si in the MA1 record. These peaks occur at and after 4.216, 2.978, 2.291, and 0.853 kyrs BP. Our geochemical fingerprinting based on EPMA data of preserved glass shards (Fig. 3b, c) and its characteristic Si/Zr ratio of about 3300[7,8] (Fig. 5) identify this ash component as Mt. Burney glass at 4.216, 2.291, and 0.853 kyrs BP. Only for the section around 2.978 kyrs BP, when the Aguilera A_1 eruption is known to have occurred, our LA-ICP-MS measurements did not identify a pristine glass component with high Si and Zr content and a Si/Zr ratio of 3600[8] that could indicate the presence of volcanic glass from Aguilera.

Furthermore, the presence of tephra fragments in the stalagmite is verified by SEM micrographs of particles extracted from the speleothem (Figs. 7a–c and S2). The structure of observed shards and vesicle-rich glass coatings on phenocrysts resemble characteristics of the well-documented Mt. Burney tephra[1,7,8,13,36]. Indications of recurring tephra input over a time span of 70 years are found also directly after these ashfall events

by continuously elevated Zr and Si contents that are well above $CaCO_3$ background values at 4.20, 4.18, 4.14, 2.94, 2.26, 2.20, 2.19, 0.79, and 0.77 kyrs BP (Fig. 5). This extended input of Zr and Si is most likely related to the deposition of fine-grained ash particles (nanotephra) that cannot be resolved by optical microscopy observations in the $CaCO_3$ matrix. Higher input of such fine-grained glass following the eruption events over decades can be explained by repeated periods of increased tephra reworking and mobilization into the aquifer during distinct phases characterized by storm-related high rainfall[9,27]. These periods coincide with decreased $\delta^{18}O$ and $\delta^{13}C$ values, which is in accord with higher precipitation rates[25] at that time. Owing to differences in Late Holocene rainfall[29] shown by variable $\delta^{18}O$ and $\delta^{13}C$ levels[25], a climate-induced influence on the hydrological soil-to-stalagmite transport is suggested, explaining the slightly dissimilar response to tephra fallout recorded by stalagmite MA1 during 4.5–4.0, 3.1–2.9, 2.4–2.0 and 0.9–0.7 kyrs BP (Figs. 3 and 4).

Micrometer-sized volcanic glass fragments with surface alteration rims were also observed by NanoSIMS (Fig. 7d–f). These particles differ considerably from crystalline, bedrock-derived silicate grains (Fig. 8c) with respect to their texture and $^{28}Si^-$ and $^{16}O^-$ secondary ion count levels at their location, which asserts them as volcanic glass. This is in accord with an expected low $^{27}Al^{16}O^-$ signal and $^{56}Fe^{16}O^-$ counts near to zero for vitreous material, which does not exclude that they contain greater amounts of Al or Fe[42,43]. The rims rich in $^{27}Al^{16}O^-$ around these particles suggest the formation of amorphous, secondary alumino-silicate phases with higher ionization rates in comparison with more crystalline structures[43–45]. We interpret the $^{12}C^-$ and $^{12}C^{14}N^-$ signals detected on the particles as reflecting enrichments of OM[42] in abundant micro-vesicles. This is consistent with the results of recent studies that documented pronounced glass leaching and the subsequent formation of Al-(hydr)oxides related to tephra weathering in other humid and acidic environments elsewhere[16,46,47]. The close textural relation between $^{27}Al^{16}O^-$ enrichments and OM ($^{12}C^-$, $^{12}C^{14}N^-$, and $^{32}S^-$[48,49]) surrounding the observed particles (Fig. 7d–f) suggests that leaching processes, e.g., microbially mediated weathering, also occur in-situ within the bio-chemical micro-environment existing at the stalagmite surface after the deposition of the tephra particles. Based on microscopic observations, we suggest that the tephra may have been fragmented mechanically while passing through 40 m of the fractured aquifer system. Subsequently, residual vitreous particles accumulated together with soil-derived OM in small pools formed at the stalagmite surface (Fig. S5e). In these accumulation pools, glass dissolution by microbes[50,51] is probably encouraged. A thin glaze of $CaCO_3$ that differs from the surrounding calcite fabric preserved the organic and inorganic components within these bio-geochemical micro-environments (Fig. S5e).

Our data constrain the chemical signals from tephra deposition: Apart from the direct observation of pristine glass shards and their in-situ alteration products, there is also evidence of secondary effects in soils as a response to volcanic fallout. Various
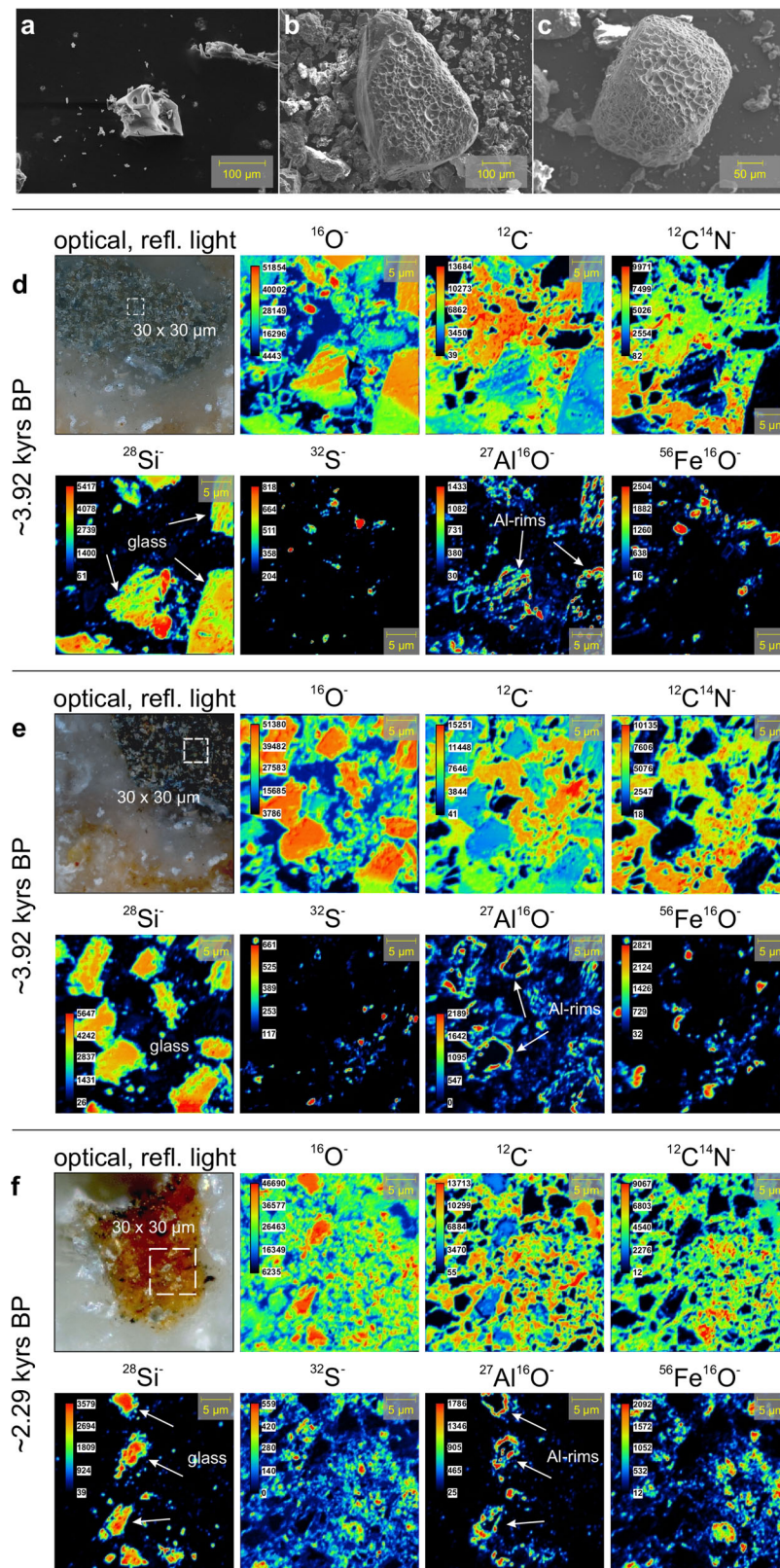
Fig. 7 Glass shards and phenocrysts from Mt. Burney tephra detected in laminae of MA1. SEM micrographs show a glass shard (**a** 2.20 kyrs BP) and phenocrysts coated with residual, vesicle-rich volcanic glass (**b**, **c** 4.15 kyrs BP) incorporated in MA1. **d–f** NanoSIMS secondary ion mappings indicate the presence of more intact fine-grained glass fragments framed by rims of elevated $^{27}Al^{16}O^{-}$ counts in OM-rich accumulation pools from laminae at ~3.92 and ~2.29 kyrs BP.
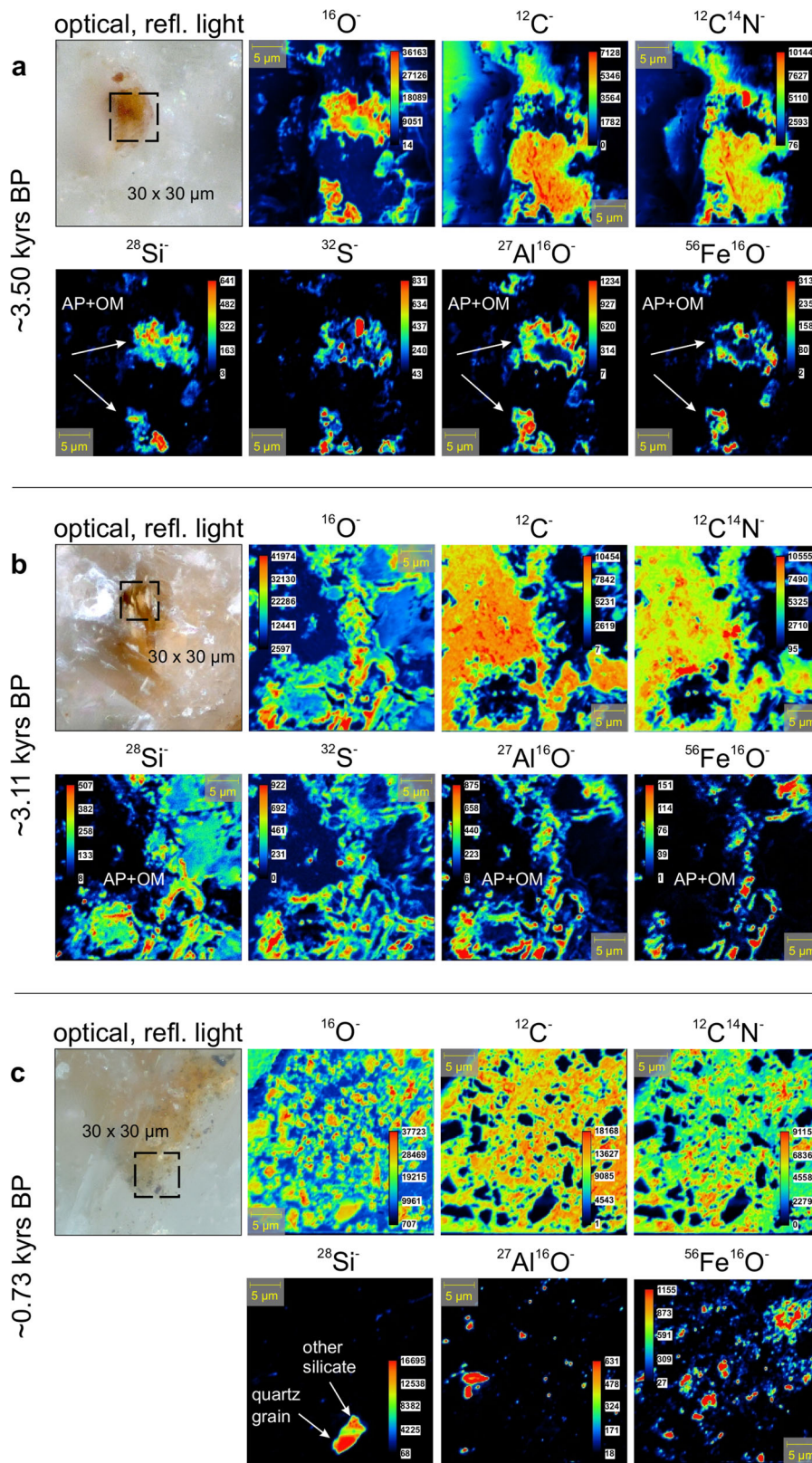
Fig. 8 NanoSIMS secondary ion mappings of detritus-rich lamina sections at ~3.50, ~3.11, and ~0.73 kyrs BP. a, **b** Alteration products (AP + OM) deposited during the millennium-scale acidification phase following the MB$_2$ eruption[1]. In both cases, at ~3.50 (**a**) and ~3.11 (**b**) kyrs BP, $^{16}O^-$, $^{28}Si^-$, $^{27}Al^{16}O^-$, $^{56}Fe^{16}O^-$ ion counts indicate that silica gels and Al-/Fe-(hydr)oxides from the catchment were incorporated together with OM ($^{12}C^-$ and $^{12}C^{14}N^-$). **c** Bedrock-derived silicates from laminae at ~0.73 kyrs BP with significantly high $^{16}O^-$ and $^{28}Si^-$ secondary ion counts. Here, $^{27}Al^{16}O^-$ and $^{56}Fe^{16}O^-$ show a completely different spatial distribution compared to **a**, **b** or more intact glass shards displayed in Fig. 7.

volcanogenic chemical compounds dissolve rapidly in surface environments after the direct wet deposition of acid rain from the eruption plume and/or after leaching by water from freshly deposited tephra[15,38]. Typical chemical compounds leached from pristine tephra are sulfates and a range of soluble salts containing other mobile and volatile metals[38]. Here we focus on S, P, Sr, and U to trace solutes potentially derived from Mt. Burney and Aguilera tephra for which the composition is well known[7,8,36].

Amongst elements released from volcanic ash after deposition, S and Sr but also P are known to reach high concentrations in surface waters[38] and U was also efficiently applied to document long-term leaching after the MB_2 eruption[1]. The low pH of 3.9–5.4 in soils of the MA catchment[26] promotes the mobilization of water-soluble elements from volcanic glass[15,17,38]. We, therefore, interpret the short-term release of Sr and U as a signal of tephra leaching in acidic waterlogged peat soils[1,14] at 4.216, 2.978, 2.291, and 0.853 kyrs BP (Figs. 3 and 4). We associate the periodically increasing Sr and U concentrations in periods following the eruptions with the storm phase-induced incorporation of (i) leached elements from tephra in the catchment or (ii) glass and its weathering residues. The high peaks of Sr could additionally be explained by a contribution from plagioclase phenocrysts[21,22] embedded in MA1 (e.g., glass-coated phenocrysts; Fig. 7b, c), which are—next to volcanic glass—a dominant component of tephra from Mt. Burney and Aguilera[7,36].

These chemical signals also determine the high amplitude spikes of PCs 1–3 (Figs. 6 and S1). We use our PCA results (Figs. 6 and S1 and Table S2) to discriminate different compositional domains in stalagmite MA1. PC-1 mainly reflects high concentrations of presumably volcanogenic SO_4^{2-} and PO_4^{3-}[15,18,22]. We expect a simultaneous mobilization of S- and P-bearing species adsorbed to or contained in pedogenic OM[52,53] due to the perturbation of peat soil hydro-chemistry after ashfall[1,2,41]. Accordingly, high amounts of $^{32}S^-$, $^{12}C^-$, and $^{12}C^{14}N^-$ secondary ions counts are correlated (Figs. 7 and 8) and imply a direct linkage between soil OM and S in the stalagmite[48,54–56] even though OM is obviously not directly associated with the composition of fresh tephra[38]. In addition, PC-1 implies a relatively high contribution of siliciclastic components in the form of fine-grained detritus in combination with intense leaching, mobilization, and deposition of mobile lithophile elements from rock substrate or tephra in soils. PC-2 and PC-3 primarily mirror leaching processes and siliciclastic components without a concurrent deposition of volcanogenic SO_4^{2-} and PO_4^{3-}. According to Jamieson et al.[22], volcanic signals in a speleothem do not automatically produce a clear corresponding chemical excursion in the stalagmite stratigraphy. However, in our particular case, all three PCs are indicative of volcanic impacts on the soil-to-stalagmite transfer and deposition system in the form of pristine glass, elements leached from the eruption plume, or products issuing from tephra alteration. As would be expected from loadings of PC-1, the main spikes of the PC-1 record coincide with peaks of the lithophile elements (Si, Sr, Zr, and U) as well as S and P concentrations (Figs. 3–5). Such high amplitude compositional spikes, significantly exceeding average concentrations, are comparable to characteristic volcanogenic signals observed in other speleothem records[18,20–23]. Therefore, it is reasonable to infer that these distinct compositional peaks mark times of trace element mobilization related to volcanic events that occurred at 4.216, 2.978, 2.291, and 0.853 kyrs BP (Figs. 3–6 and S1).

Chemical signals appear to indicate a prolonged chemical footprint of tephra deposition (i.e., elevated Si, Sr, and Zr; Figs. 3–5) in speleothem laminae from 3.8 to 3.0 kyrs BP, similar to that at 4.216, 2.978, 2.291, and 0.853 kyrs BP. However, there is no direct evidence for tephra deposition from nearby Mt. Burney, Reclus, or Aguilera volcanoes at that time[3,5,8]. Despite our

intensive search by optical microscopy, wavelength dispersive spectroscopy (WDS) element mapping, and SEM, we could not detect any intact vitreous particles between 3.8 and 3.0 kyrs BP. The measured compositions of Si-rich particles from this section of MA1 cannot be associated with the composition of fresh volcanic glass or stoichiometric basement-derived minerals (Fig. 3d and Table S5). Alkali metal contents are exceedingly low and pronounced Al-/Fe-(hydr)oxide enrichment, as suggested by high Al_2O_3/TiO_2 and FeO/TiO_2 ratios, is observed. We, therefore, categorize these high Al-Fe-Si compounds to be the result of glass decomposition where newly formed alteration products were partly mixed with surrounding $CaCO_3$ (higher CaO values during EPMA analysis).

Based on our data, we argue that the environmental impact on soils from volcanic depositions is modulated by climate variations. Kilian et al.[1] documented a millennial-scale acidification phase in regional soils following the Plinian MB_2 eruption. This may have caused efficient chemical alteration of tephra and transport of leached elements from the catchment onto the speleothem. Accordingly, we observe correlated patterns of $^{12}C^{14}N^-$, $^{32}S^-$, $^{28}Si^-$, $^{27}Al^{16}O^-$, and $^{56}Fe^{16}O^-$ counts in NanoSIMS images of the speleothem during the period following the MB_2 eruption (Fig. 8a, b). This indicates the accumulation of silicate weathering products together with OM[44,48,49]. These weathering products are typical for the decomposition of vitreous tephra in acidic soils and are likely comprised of organo-mineral complexes enriched in Al-/Fe-(hydr)oxides and silica gels[46,47]. These compounds preferentially form in highly reactive aquatic redox environments[57] subjected to such extremely variable climate conditions[28,30].

We also observe variations of $\delta^{18}O$ and $\delta^{13}C$ values[25] by 1–1.5‰ in the record following the events at 4.216, 2.978, 2.291, and 0.853 kyrs BP. First, the $\delta^{18}O$ and $\delta^{13}C$ values decrease for ca. 10 years followed by higher values lasting for ~20 years (Fig. 4). We interpret these isotopic changes as a combined effect of varying rainfall intensity and short-term perturbations of the hydro-chemical soil system within the catchment—subsequent to and genetically related to events of tephra deposition[21]. Environmental changes such as variations in redox-pH conditions, water-table fluctuations, and nutrient release from ash deposition may strongly affect plant decomposition, and thus, the delivery of dissolved organic matter (DOM) and organo-mineral compounds from peat soils[57–59]. The DOM then can percolate into cave drip waters and be recorded by the $\delta^{13}C$ signatures of speleothems[20,54–57]. A close relationship between the abundance of OM that derives from DOM or mineral-associated OM in the drip water and $^{12}C^-$, $^{12}C^{14}N^-$ and $^{32}S^-$ signals in detritus-rich laminae of MA1 is shown by the NanoSIMS measurements[48,49] (Figs. 7 and 8). Therefore, a link between detrital and volcanic input in MA1 and the fundamental changes in soil chemistry and hydrology in the catchment is clearly established.

Finally, an import of elements such as S and Sr in the MA catchment area can also occur by sea salt aerosols[25,60,61]. It is known that sea salt contribution from the nearby Pacific Ocean through surface deposition and transfer to cave drip waters is responsible for overall elevated concentrations compared to more continental speleothems[21,22,24,25,62]. Such speleothems contain concentrations of, i.e., Sr ranging between 10 and 20 ppm[22,62]. Consistent and strong SWW-induced wind velocities and frequent storm events in the region[9,27] cause a constant deposition of sea spray-derived elements. These elements are characterized by short residence times in waterlogged peatland soils[14], and thus, we argue that the high annual precipitation[9,28,30] leads to a persistent input of excess sea salt S and Sr signatures in MA1 compared to other speleothems. Therefore, sea salt-derived S and Sr contribution should be of secondary importance for the

distinct high amplitude spikes of these elements. Their deposition would not result in the documented compositional spikes and a close correlation that we observe with other mobile and immobile lithophile trace elements (e.g., Si, U, and Zr, Figs. 3–5) would not be expected.

Using the evidence from primary and secondary volcanic signals in the speleothem record, these data have implications for tephrochronology because our results prove that the MA1 stalagmite recorded distinct volcanic events for which we can determine precise ^{230}Th/U-ages from the refined age-depth model based on the StalAge algorithm[29] with errors represented by 95% confidence limits (Fig. 2a). Our speleothem record shows no distinct hiatus and because of the proximal location and high temporal resolution, it also comprises volcanogenic signals from so far insufficiently dated, notably smaller Mt. Burney eruptions with unknown ash dispersal and regional environmental impact (MB_3 and MB_4). It is important to note that — apart from stratigraphic correlation — a differentiation between fresh ash depositions and rainfall-induced soil erosion/reworking of older tephra layers[1,63] is necessary. Evidence for a distinct major tephra reworking event is high peaks of Si and Zr without the recording of a compositional volcanic signal at the same time. In addition, phases of increased reworking should also correlate with paleo-precipitation data (δ^{18}O and δ^{13}C) and known past environmental conditions. For instance, a major reworking event is recorded during the termination of a well-documented cold phase[9] at ~2.5 kyrs BP. Due to the environmental damage caused by the millennium-scale acidification[1] and the subsequent cold phase[9], a series of storm events with extreme rainfall may have mobilized MB_2 ash from bare, sparsely vegetated surfaces at that time (Fig. S3). With respect to the rapid alteration of volcanic glass in acidic soils under humid climate[64], the reworked material from older, surface-near tephra should not contain pristine glass and high S concentrations would not be expected. Indeed, the peaks of S at ~2.5 kyrs BP are considerably reduced by a factor of ten in comparison with the distinct volcanic events that we detected (Fig. 3). Accordingly, the LA-ICP-MS data from a section older than the MB_2 eruption (4.8–4.6 kyrs BP) indicate similar depositional events comprising Mt. Burney ash (Fig. S4). Unlike the other tephra signals discussed above, no published ^{14}C-ages exist for this time, and thus, a correlation with a Mt. Burney eruption would be highly speculative. However, a possible eruption of Mt. Burney (MBK_3[3]) was identified based on a 1 mm thick tephra layer found in only one local sediment core with a ^{14}C-age of >4.96 ± 0.09 kyrs BP[13]. Here, further interpretations with respect to primary ashfall or reworked inputs must await a more detailed analysis of this oldest section of MA1.

We consider the most important findings of this study that, based on ^{230}Th/U-ages, three Mt. Burney eruptions can now be dated more accurately to 4216 $^{+93}/_{-193}$ yrs BP (MB_2), 2291 ± 33 yrs BP (MB_3), and 853 $^{+41}/_{-60}$ yrs BP (MB_4). The ^{230}Th/U-age for the MB_2 eruption is in good agreement with the ^{14}C-age of 4200 ± 50 cal yrs BP published by Breuer et al.[63], which is based on macro-plant remains included in the >10 cm thick MB_2 ash deposit. Our new MB_3 age falls into the lowermost range of bracketing ^{14}C-ages presented by Biester et al.[12] and Kilian et al.[13]. In both papers, the MB_3 eruption was roughly dated to ~2020 ± 90 cal yrs BP (>1830 ± 40 and <2210 ± 90 cal yrs BP[12], >1980 ± 40 and <2060 ± 90 cal yrs BP[13]). This new age is, therefore, more precise than previous datings. A further Mt. Burney eruption (MB_4) that was only tentatively dated through stratigraphic correlation (~800 yrs BP[65]) is now more precisely dated to 853 $^{+41}/_{-60}$ yrs BP, based on the data of this study.

Following our arguments developed above, our trace element profiling and PCA analysis (Figs. 3–6 and S1), indicate that an additional volcanic event occurred at a ^{230}Th/U-age of 2978

$^{+91}/_{-104}$ yrs BP. This event could not be linked to a specific eruption by chemical correlation of tephra because no glass was detected in MA1 at this time. However, the A_1 eruption from the remote Aguilera stratovolcano has a poorly defined ^{14}C-age bracketed between ~3067 and 3339 cal yrs BP[7] and, therefore, it is the most likely candidate for this event. This is in accordance with the regional distribution of A_1 tephra[7], which has also been discovered in lacustrine sediments nearby the MA cave site[13].

With this successful identification of volcanic eruptions, we propose that our high-resolution speleothem archive enable precise ^{230}Th/U-age constraints for a refinement of existing tephrochronologies, closing a significant gap in the reconstruction of the volcanic activity in South Patagonia. Potentially, the variations in LA-ICP-MS trace element concentrations in this stalagmite imply environmental impacts induced by further ashfall events from more distal volcanic centers of the Southern and Austral Volcanic Zones but are much more difficult to detect. For example, there are peaks of elevated S concentrations in MA1 (Figs. 3 and 4) at times when no eruption is documented by the nearby volcanoes. These distinct S peaks likely record atmospheric signals of more distant volcanoes, such as Reclus and Cerro Hudson and, potentially, other high-magnitude volcanic events in the southern hemisphere off South America. This opens the possibility of correlation with Antarctic ice cores[66] to evaluate large-scale southern hemispheric patterns of Late Holocene volcanism.

We, therefore, conclude that the unique, sub-annually resolved speleothem LA-ICP-MS data presented here may constitute an important advancement in our knowledge about the Late Holocene tephrochronology of southernmost South America. This will allow a better understanding of the volcanic history in the region, and an improvement for the reconstruction of paleoclimate and paleoenvironmental conditions from regional geological archives. Besides well-preserved tephra layers, MA1 provides multiple climatically and environmentally important information due to its unique nature as a non-karst stalagmite with enclosed organic and inorganic detrital components. This information includes potential feedback signals to SWW dynamics and environmental impacts of regional volcanism back to ~4.8 kyrs BP, documenting the evolution of one of the most remote and pristine ecosystems worldwide[9,27].

Methods

Chronology. Stalagmite MA1 was dated at the Heidelberg Academy of Sciences. Sample preparation and analytical methods were described in detail by Schimpf et al.[25]. We included two additional samples (Lab. No. 3672 and 3436, Table S1) that were not considered in Schimpf et al.[25] due to their large content of detrital ^{232}Th. Stalagmite MA1 generally contains high amounts of detrital Th. This is obvious from the ^{230}Th/^{232}Th activity ratios that range from 4.257 to 93.70 (Lab. No. 3672 and 3653, Table S1). However, these values are well below the limit of >200 suggesting insignificant detrital contamination[67]. Detrital contamination of MA1 also results in age inversions (i.e., uncorrected ages that are not in stratigraphic order). For instance, the sample with Lab. No. 3435 at 268.5 mm distance from the top (dft) is significantly older (5.128 kyrs BP) than the sample below at 274 mm dft (4.803 kyrs BP).

Schimpf et al.[25] assumed a ^{232}Th/^{238}U weight ratio of 4.8 ± 50% for the detritus, which resulted in a smooth age-depth relationship. This value agrees with the conventionally used value for the upper continental crust (3.8 ± 1.9[68]). Here we used a different approach to account for detrital contamination, based on an algorithm recently published by Budsky et al.[35]. This algorithm calculates corrected ages assuming a specific ^{232}Th/^{238}U weight ratio of the detritus and ^{230}Th, ^{234}U, and ^{238}U in secular equilibrium, and then determines the ^{232}Th/^{238}U weight ratio of the detritus, which results in a minimum sum of age inversions (in years). For stalagmite MA1, this approach results in a ^{232}Th/^{238}U weight ratio of the detritus of 3.69, which is close to the mean value of the upper continental crust[68] and in agreement within the error with the value used by Schimpf et al.[25]. As suggested by Budsky et al.[35], we assumed a conservative uncertainty of ±50% for the determined ^{232}Th/^{238}U ratio of the detritus. Figure 2a shows a comparison of the uncorrected and the corrected ages.

The final age-depth model for MA1 (Fig. 2a) was calculated in R[69] using the Monte-Carlo-based StalAge algorithm[34], which has been specifically designed for speleothems. In contrast to the previously used Akima interpolation, StalAge

provides 95% confidence limits, which allows to assess the uncertainty of the age model.

Drip water pH. The pH of cave drip water collected at the MA1 sampling site was measured on-site with a digital pH-meter during expeditions between 2006 and 2008.

Mineralogical analyses. The mineral composition of a powdered specimen from ~37 mm dft (Fig. S2g) was identified by X-ray diffraction with a Siemens D500 X-ray diffractometer at the Geology Department of Trier University. The diffractogram was evaluated using the DIFFRAC plus 5.0 software from Bruker. We accepted the calcite peak at 3.036 Å (Cu-Kα radiation) as the internal standard.

LA-ICP-MS data. The MA1 stalagmite was analyzed with laser ablation inductively coupled plasma mass spectrometry (LA-ICP-MS) at GZG, University of Göttingen. LA-ICP-MS elemental analyses were performed as two parallel ablation tracks on 14 overlapping, 30 μm thick and 40–50 mm long polished thin sections covering the growth axis of the stalagmite from 24 to 280 mm dft (Fig. S5a). This approach accounts for lateral heterogeneities with respect to small-scale differences during stalagmite growth. We used the same thin sections as for EPMA presented in Schimpf et al.[25]. Figure S6 documents that the resin used for thin section manufacturing does not contain S, P, U, Sr, Si, or Zr in any significant amounts. Therefore, potential contamination caused by adhesive compounds affecting the LA-ICP-MS element concentrations presented in this study can be excluded. The ICP-MS used was a Perkin Elmer ELAN DRC II Q-ICP-MS coupled to a Lambda Physik COMPex 110 Argon Fluoride laser (193 nm) with a GeoLas optical bench by MikroLas and a small volume sample chamber. The ablation setup was operating with a beamwidth of 120 μm, a repetition rate of 10 Hz for the laser pulses (dwell time 40 ms per isotope, 1.078 s per sweep), and a scan speed of 20 μm s^{-1}. Background data were taken before and after the measurements for 2–3 min. The measurements were calibrated to the standards NIST610 and NIST612 by bracketing analyses and the internal standard ^{43}Ca was used to convert the measurements into absolute concentrations. Matrix effects between NIST610/NIST612 and CaCO$_3$ were considered to contribute less than 10% error. Measured isotopes were ^{27}Al, ^{29}Si, ^{31}P, ^{34}S, ^{43}Ca, ^{88}Sr, ^{90}Zr, and ^{238}U. Element concentrations have been normalized to the stoichiometric 400,000 ppm ^{43}Ca, assuming that the stalagmite is composed of 100% CaCO$_3$. The background was subtracted and baseline drift corrected. For ablation spots on lamina with more than 10% detrital siliciclastic material (minerals/volcanic glass containing considerably lower Ca compared to speleothem CaCO$_3$), the internal normalization to ^{43}Ca will result in systematically higher values for lithophile elements. However, their elemental ratios (e.g., Si/Zr) will be unaffected. The analytical background of Si (<5,000 ppm) and Zr (<3 ppm) represents analytical scatter at low concentrations, and possibly, a weak signal caused by continuous tephra input from reworking. This background range was defined based on the limits of detection for Si and Zr[70] and the observed scatter in our LA-ICP-MS data set.

The final LA-ICP-MS record was compiled by aligning the overlapping ablation tracks using a wiggle-matching technique based on the Al concentrations measured — taking small-scale variations of lamina thickness into account. It is characterized by sub-annual resolution in total 59,200 LA-ICP-MS measurements covering a time span of 4212 years (4809–597 yrs BP). Finally, the consistency of the LA-ICP-MS data set with already published ICP-MS drill core data[25] was ensured by matching averaged concentrations of the LA-ICP-MS measurements with the contents previously determined by ICP-MS. For this purpose, we chose U as soluble, calcite-compatible element[25] and used the original drilling diameter of 1.5 mm in accordance with the exact distance from the top for every single coring point to calculate the average of the LA-ICP-MS concentrations for comparison (~290 LA-ICP-MS measurements per drill core). The LA-ICP-MS and ICP-MS U concentrations are in good agreement and correlate with $r = 0.68$ (Fig. S7).

The principal component analyses (PCA) for the assessment of speleothem high-resolution LA-ICP-MS data was done according to Orland et al.[37] and Jamieson et al.[22]. The PCA was performed with Origin (version Pro 2019b) to further constrain the occurrence of signals in MA1 derived from volcanic activity and was calculated for the trace elements P, S, Sr, Si, Zr, and U after z-score normalization.

EPMA analyses of silicate components in MA1. The major element compositions of silicate minerals and glass shards incorporated in laminae of MA1 that formed at 4.216, 2.291, 0.853 kyrs BP and shortly after were measured using a JEOL JXA-8900 RL EPMA equipped with five WDS spectrometers at GZG, University of Göttingen. On the polished thin sections, areas of interest (AOIs) with embedded silicates (Fig. S5d, e) in porous fabrics were selected by (i) optical microscopy, (ii) SEM imagery, and (iii) WDS elemental mappings of Si, Al, and Fe (15 kV acceleration voltage, a beam current of 60 nA, 6 μm beam diameter, and a grid of 500 × 500 steps, step size of 6–8 μm, and 60 s dwell time/step). Quantitative individual silicate analyses were performed at an acceleration voltage of 15 kV and a beam current of 15 nA. Depending on the size of the particles, the beam diameter was adapted between 2 and 10 μm. The counting times of the characteristic X-ray signals were chosen between 8 and 10 s (Na, K), 15 s (Si, Al, Mg, Ca, Fe), and 30 s

(Ti, Mn, P). The known effect of alkali-loss under electron bombardment has been checked and was found to be insignificant. For measurements on small grains, counting times of Na and K were reduced to 8 s. Natural (wollastonite: Si, Ca; anorthite: Al; hematite: Fe; olivine: Mg; rhodonite: Mn; albite: Na; sanidine: K) and synthetic (TiO$_2$: Ti; ScPO$_4$: P) reference materials were used for primary calibration. Routine analyses on secondary standards were performed on the two reference glasses VG-2 and NKT-1G (see Table S6 for details). Matrix correction was applied by using the phi-rho-z algorithm of the CITZAF program[71]. We discarded glass measurements that contain more than 80 wt.% SiO$_2$ after normalization to 100 wt.%.

SEM and NanoSIMS of incorporated detrital components. Stalagmite sections formed during and after the two Plinian eruption periods of the Mt. Burney volcano at 2.3–2.0 kyrs BP, 4.2–3.8 kyrs BP and during the millennium-scale acidification phase (~3.50 and ~3.11 kyrs BP) after the MB$_2$ eruption[1], and at ~0.73 kyrs BP include laminae rich in detrital components. Representative samples have been investigated with SEM and NanoSIMS. These samples contain the same detritus-rich laminae as analyzed by LA-ICP-MS. We chose NanoSIMS because this technique allows to differentiate embedded inorganic (e.g., ^{28}Si$^-$, ^{27}Al^{16}O$^-$) and organic (e.g., ^{12}C^{14}N$^-$) components from ubiquitous, very low electrically conductive CaCO$_3$[72,73].

SEM imaging was conducted with a LEO 435VP and a JEOL JXA-8900 RL at the Geology Department of Trier University and the GZG, University of Göttingen. Replicate samples were analyzed (i) on thin sections and (ii) after dissolution in 5 M ultra-pure HCl and an acidic acetate buffer solution[74] to extract incorporated detritus from distinct laminae. An acceleration voltage of 15 kV was applied to produce high-resolution images in secondary electron and back-scattered electron mode.

Samples for NanoSIMS analyses were taken from the identical blocks the thin sections were prepared of (Fig. S5a). Prior to NanoSIMS measurements, the sample documentation and the selection of AOIs was guided by optical microscopy. We preferentially chose porous laminae, in which abundant organic and inorganic components are embedded in transition zones of different fabrics, so-called accumulation pools (Fig. S5d). NanoSIMS analyses were carried out at the Chair of Soil Science of the Technical University of Munich with a Cameca NanoSIMS 50 L using a Cs$^+$ primary ion beam with an impact energy of 16 keV. The selected stalagmite samples were polished and coated with a conductive Au/Pd layer (ca. 30 nm, Polaron Emitech SC7640 sputter coater) to account for charging during the measurements. Charging was additionally compensated using the electron flood gun of the NanoSIMS. Contaminants and the Au/Pd coating layer were locally sputtered away using a high primary beam current (pre-sputtering/implantation), while the reactive Cs$^+$ ions were implanted into the sample. The secondary ion yields were enhanced until reaching a steady state. The primary beam (ca. 2 pA) was focused at a lateral resolution of ca. 120 nm and was scanned over the sample, with ^{12}C$^-$, ^{16}O$^-$, ^{12}C^{14}N$^-$, ^{28}Si$^-$, ^{32}S$^-$, ^{27}Al^{16}O$^-$, and ^{56}Fe^{16}O$^-$ secondary ions collected on electron multipliers with an electronic dead time fixed at 44 ns. Due to the pure Cs$^+$ ionization, positively charged ions, such as ^{14}N$^+$, ^{27}Al$^+$, and ^{56}Fe$^+$, were measured in combination with C$^-$ and O$^-$ ions, respectively[43,49]. To accurately separate mass isobars, a suitable mass resolution was achieved with appropriate slits and apertures (D1_3, ES_3, AS_2). The secondary ions were recorded using a dwell time of 1 ms pixel^{-1}, with 256 × 256 pixels for a 30 × 30 μm field of view with 30 planes per scan. Single planes were corrected for dead time, drift, and accumulated using the ImageJ software[75] in combination with the Open-MIMS plugin[76].

The sensitivity of SIMS spans more than five orders of magnitude and the SIMS secondary ion yield notably depends on the ionization potential and the electron affinity of each species[73]. The secondary ion intensities do not reflect the relative element concentrations of the sample since different species have largely different ionization probabilities[42]. Furthermore, the ionization probability is very specific to the composition and chemistry of the surrounding matter, the so-called matrix effect[73]. Due to this effect, the ion yield of one element can be enhanced while the ion yield of another element can be suppressed under the same sputtering conditions[49,73]. Caution is therefore needed when interpreting NanoSIMS data on a specific mineral phase. As the count rate of an ion is not directly proportional to the elemental concentration in the mineral, a linear interpolation based on its elemental concentration is not expected[42,43].

Data availability
The data sets generated during the current study can be obtained from the Zenodo repository (https://doi.org/10.5281/zenodo.5856380). The LA-ICP-MS data may also be found in the online version of this article (Supplementary Data 1).

References

1. Kilian, R. et al. Millennium-scale volcanic impact on a pristine and superhumid ecosystem. *Geology* **34**, 609–612 (2006).
2. Loisel, J. & Bunsen, M. Abrupt fen-bog transition across Southern Patagonia: timing, causes and impacts on carbon sequestration. *Front. Ecol. Evol.* **8**, 273 (2020).
3. Fontjin, K. et al. Late Quaternary tephrostratigraphy of southern Chile and Argentina. *Quat. Sci. Rev.* **89**, 70–84 (2014).
4. Lowe, D. Tephrochronology and its application: a review. *Quat. Geochronol.* **6**, 107–153 (2011).
5. Smith, R. E. et al. Refining the Late Quaternary tephrochronology for southern South America using the Laguna Potrok Aike sedimentary record. *Quat. Sci. Rev.* **218**, 137–156 (2019).
6. Stern, C. R. Active Andean volcanism: Its geologic and tectonic setting. *Rev. Geol. Chile* **31**, 161–206 (2004).
7. Stern, C. R. Holocene tephrochronology record of large explosive eruptions in the southernmost Patagonian Andes. *Bull. Volcan.* **70**, 435–454 (2008).
8. Del Carlo, P. et al. Late Glacial-Holocene tephra from southern Patagonia and Tierra del Fuego (Argentina, Chile): a complete textural and geochemical fingerprinting for distal correlations in the Southern Hemisphere. *Quat. Sci. Rev.* **195**, 153–170 (2018).
9. Kilian, R. & Lamy, F. A review of Glacial and Holocene paleoclimate records from southernmost Patagonia (49-55°S). *Quat. Sci. Rev.* **53**, 1–23 (2012).
10. Yu, S.-Y., Shen, J. & Colman, S. M. Modeling the radiocarbon reservoir effect in lacustrine systems. *Radiocarbon* **49**, 1241–1254 (2007).
11. Bertrand, S., Hughen, K. A., Sepulveda, J. & Pontaja, S. Geochemistry of surface sediments from the fjords of Northern Chilean Patagonia (44 – 47°S): Spatial variability and implications for paleoclimate reconstructions. *Geochim. Cosmochim. Acta* **76**, 125–146 (2012).
12. Biester, H. et al. Elevated mercury concentrations in a peat bog of the Magellanic Moorlands, Chile (53°S) – an anthropogenic signal? *Earth Planet. Sci. Lett.* **201**, 609–620 (2002).
13. Kilian, R. et al. Holocene peat and lake sediment tephra record from the southernmost Andes (53-55°S). *Rev. Geol. Chile* **30**, 47–64 (2003).
14. Martini, I. P., Martínez-Cortizas, A. & Chesworth, W. (eds) in *Developments in Earth Surface Processes* 9 (Elsevier Amsterdam, 2006).
15. Jones, M. T. & Gislason, S. R. Rapid release of metal salts and nutrients following the deposition of volcanic ash into aqueous environments. *Geochim. Cosmochim. Acta* **72**, 3661–3680 (2008).
16. Opfergeld, S. et al. Iron and silicon isotope behavior accompanying weathering in Icelandic soils, and the implications for iron export from peatlands. *Geochim. Cosmochim. Acta* **217**, 273–291 (2017).
17. Pearce, N. J. G., Alloway, B. V. & Wickham, C. Correlating weathered, microphenocryst-rich, intermediate tephra: An approach combining bulk and single shard analyses from the Lepué tephra, Chile and Argentina. *Quat. Int.* **500**, 71–82 (2019).
18. Frisia, S., Borsato, A. & Susini, J. Synchrotron radiation applications to past volcanism archived in speleothems: an overview. *J. Vol. Geo. Res.* **177**, 96–100 (2008).
19. Frisia, S. et al. The influence of Antarctic subglacial volcanism on the global iron cycle during the Last Glacial Maximum. *Nat. Commun.* **8**, 15425 (2017).
20. Siklósy, Z. et al. Bronze Age volcanic event recorded in stalagmites by combined isotope and trace element studies. *Rapid Commun. Mass Spectrom.* **23**, 801–808 (2009).
21. Badertscher, S. et al. Speleothems as sensitive recorders of volcanic eruptions – the Bronze Age Minoan eruption recorded in a stalagmite from Turkey. *Earth Planet. Sci. Lett.* **392**, 58–66 (2014).
22. Jamieson, R. A., Baldini, J. U. L., Frappier, A. B. & Müller, W. Volcanic ash fall events identified using principal component analysis of a high-resolution speleothem trace element dataset. *Earth Planet. Sci. Lett.* **426**, 36–45 (2015).
23. Paine, A. R. et al. The trace-element composition of a Polish stalagmite: Implications for the use of speleothems as a record of explosive volcanism. *Chem. Geol.* **570**, 120157 (2021).
24. Frisia, S., Borsato, A., Fairchild, I. J. & Susini, J. Variations in atmospheric sulphate recorded in stalagmites by synchrotron micro-XRF and XANES analyses. *Earth Planet. Sci. Lett.* **235**, 729–740 (2005).
25. Schimpf, D. et al. The significance of chemical, isotopic, and detrital components in three coeval stalagmites from the superhumid southernmost Andes (53°S) as high-resolution palaeo-climate proxies. *Quat. Sci. Rev.* **30**, 443–459 (2011).
26. Klaes, B. et al. Middle to Late Holocene mobilization of DOC-bound Pb and Y in the Magellanic moorlands (Chile, 53°S) as a function of sea spray fertilization, climate variations and volcanic fallout? A preliminary report. *E&G Quat. Sci. J.* **67**, 1–6 (2018).
27. Lamy, F. et al. Holocene changes in the position and intensity of the southern westerly wind belt. *Nat. Geosci.* **3**, 695–699 (2010).
28. Garreaud, R., Lopez, P., Minvielle, M. & Rojas, M. Large-scale control on the Patagonian climate. *J. Climate* **26**, 215–230 (2013).
29. McCulloch, R. D. et al. Late glacial and Holocene climate variability, southernmost Patagonia. *Quat. Sci. Rev.* **229**, 106131 (2020).
30. Weidemann, S. et al. A 17 year record of meteorological observations across the Gran Campo Nevado Ice Cap in Southernmost Patagonia. *Front. Earth Sci.* https://doi.org/10.3389/feart.2018.00053 (2018).
31. Frisia, S. Microstratigraphic logging of calcite fabrics in speleothems as a tool for palaeoclimate studies. *Int. J. Speleol.* **44**, 1–16 (2015).
32. Frisia, S., Borsato, A. & Hellstrom, J. High spatial resolution investigation of nucleation, growth and early diagenesis in speleothems as exemplar for sedimentary carbonates. *Earth Sci. Rev.* **178**, 68–91 (2018).
33. Pearson, A. R., Hartland, A., Frisia, S. & Fox, B. R. S. Formation of calcite in the presence of dissolved organic matter: partitioning, fabrics and fluorescence. *Chem. Geol.* **539**, 119492 (2020).
34. Scholz, D. & Hoffmann, D. L. StalAge – an algorithm designed for construction of speleothem age models. *Quat. Geochronol.* **6**, 369–382 (2011).
35. Budsky, A. et al. Speleothem record suggests enhanced summer drought in south-eastern Spain between 9.7 and 7.5 ka – a circum-Western Mediterranean anomaly? *Holocene* **29**, 1113–1133 (2019).
36. Stern, C. R. & Kilian, R. Role of the subducted slab, mantle wedge and continental crust in the generation of adakites from the Andean Austral Volcanic Zone. *Contrib. Mineral. Petr.* **123**, 263–281 (1996).
37. Orland, I. J. et al. Seasonal climate signals (1990-2008) in a modern Soreq Cave stalagmite as revealed by high-resolution geochemical analysis. *Chem. Geol.* **363**, 322–333 (2014).
38. Ayris, P. M. & Delmelle, P. The immediate environmental effects of tephra emission. *Bull. Volcan.* **74**, 1905–1936 (2012).
39. Mohr, C. H., Korup, O., Ulloa, H. & Iroumé, A. Pyroclastic eruption boosts organic carbon fluxes into Patagonian fjords. *Glob. Biogeochem. Cycl.* **31**, 1626–1638 (2017).
40. Möckel, S., Erlendsson, E., Prater, I. & Gísladóttir, G. Tephra deposits and carbon dynamics in peatlands of a volcanic region: lessons from the Hekla 4 eruption. *Land Degrad. Dev.* **32**, 654–669 (2020).
41. Hughes, P. D. M. et al. The impact of high tephra loading on late-Holocene carbon accumulation and vegetation succession in peatland ecosystems. *Quat. Sci. Rev.* **67**, 160–175 (2013).
42. Höschen, C. et al. Novel sample preparation technique to improve spectromicroscopic analyses of micrometer-sized particles. *Environ. Sci. Technol.* **49**, 9874–9880 (2015).
43. Heister, K. et al. NanoSIMS as a tool for characterizing soil model compounds and organomineral associations in artifical soils. *J. Soil. Sediment* **12**, 35–47 (2012).
44. Mergelov, N. et al. Alteration of rocks by endolithic organisms is one of the pathways for the beginning of soils on Earth. *Nat. Sci. Rep.* **8**, 3367 (2018).
45. Lenting, C. et al. Towards a unifying mechanistic model for silicate glass corrosion. *npj Mater. Degrad.* **2**, 28 (2018).
46. Takahashi, T. & Dahlgren, R. A. Nature, properties and function of aluminum–humus complexes in volcanic soils. *Geoderma* **263**, 110–121 (2016).
47. Bonatotzky, T., Ottner, F., Erlendsson, E. & Gísladóttir, G. The weathering of volcanic tephra and how they impact histosol development. An example from South East Iceland. *Catena* **172**, 634–646 (2019).
48. Vidal, A. et al. Visualizing the transfer of organic matter from decaying plant residues to soil mineral surfaces controlled by microorganisms. *Soi.l Biol. Biochem.* **160**, 108347 (2021).
49. Mueller, C. W. et al. Advances in the analysis of biogeochemical interfaces, NanoSIMS to investigate soil microenvironments. *Adv. Agron* **121**, 1–46 (2013).
50. Hobara, S., Ogawa, H. & Brenner, R. Amino acids and amino sugars as molecular indicators of the origins and alterations of organic matter in buried tephra layers. *Geoderma* **373**, 114449 (2020).
51. Ferreiro, N., Satti, P. & Mazzarino, M. J. Biological legacies promote succession and soil development an tephra from the Puyehue-Cordon Caulle eruption (2011). *Austral. Ecol.* **43**, 435–446 (2018).
52. Novák, M., Adamová, M., Kelman Wieder, R. & Bottrell, S. H. Sulfur mobility in peat. *Appl. Geochem.* **20**, 673–681 (2005).
53. Worrall, F. et al. The total phosphorus budget of a peat-covered catchment. *J. Geophys. Res. Biogeosci.* **121**, 1814–1828 (2016).
54. Wynn, P. M. et al. Biogeochemical cycling of sulphur in karst and transfer into speleothem archives at Grotta di Ernesto, Italy. *Biogeochemistry* **114**, 255–267 (2013).
55. Li, X. et al. A 9000-year carbon isotopic record of acid-soluble organic matter in a stalagmite from Heshang Cave, central China: Paleoclimate implications. *Chem. Geol.* **388**, 71–77 (2014).
56. Blyth, J. A., Hartland, A. & Baker, A. Organic proxies in speleothems – new developments, advantages and limitations. *Quat. Sci. Rev.* **149**, 1–7 (2016).
57. Peiffer, S. et al. A biogeochemical-hydrological framework for the role of redox-active compounds in aquatic systems. *Nat. Geosci.* **14**, 264–272 (2021).
58. Dieleman, C. M. et al. Climate change effects on peatland decomposition and porewater dissolved organic carbon biogeochemistry. *Biogeochemistry* **128**, 385–396 (2016).

59. Tank, S. E., Striegl, R. G., McClellad, J. W. & Kokelj, S. V. Multi-decadal increases in dissolved organic carbon and alkalinity flux from the Mackenzie drainage basin to the Arctic Ocean. *Environ. Res. Lett.* **11**, 054015 (2016).

60. Broder, T., Blodau, C., Biester, H. & Knorr, K. H. Sea spray, trace elements, and decomposition patterns as possible constraints on the evolution of CH_4 and CO_2 concentrations and isotopic signatures in oceanic ombrotrophic bogs. *Biogeochemistry* **122**, 327–342 (2015).

61. Mathijssen, P. J. H., Galka, M., Borken, W. & Knorr, K.-H. Plant communities control long term carbon accumulation and biogeochemical gradients in a Patagonian bog. *Sci. Tot. Environ.* **684**, 670–681 (2019).

62. Borsato, A., Frisia, S., Fairchild, I. J., Somogyi, A. & Susini, J. Trace element distribution in annual stalagmite laminae mapped by micrometer-resolution X-ray fluorescence: Implications for incorporation of environmentally significant species. *Geochim. Cosmochim. Acta* **71**, 1494–1512 (2007).

63. Breuer, S. et al. Holocene denudation rates from the super-humid southernmost Patagonian Andes (53°S) deduced from lake sediment budgets. *Geomorphology* **187**, 135–152 (2013).

64. Ugolini, F. C. & Dahlgren, R. A. Soil development in volcanic ash. *Glob. Environ. Res.* **6**, 69–81 (2002).

65. Siebert, L., Simkin, T. & Kimberly, P. *Volcanoes of the World* (University of California Press, 2010).

66. Sigl, M. et al. Timing and climate forcing of volcanic eruptions for the past 2,500 years. *Nature* **523**, 543–549 (2015).

67. Richards, D. A. & Dorale, J. A. Uranium-series chronology and environmental applications of speleothems. *Rev. Mineral. Geochem.* **52**, 407–460 (2003).

68. Wedepohl, K. H. The composition of the continental crust. *Geochim. Cosmochim. Acta* **59**, 1217–1232 (1995).

69. R Core Team. The R Project for statistical computing. https://www.r-project.org (2020).

70. Wu, S., Karius, V., Schmidt, B. C., Simon, K. & Wörner, G. Comparison of ultramafine powder pellet and flux-free fusion glass for bulk analysis of granitoids by laser ablation-inductively coupled plasma-mass spectroscopy. *Geostand. Geoanal. Res.* **42**, 575–591 (2018).

71. Armstrong, J. T. CITZAF: a package of correction programs for the quantitative electron microbeam Xray analysis of thick polished materials, thin films, and particles. *Microbeam Anal.* **4**, 177–200 (1995).

72. Pacton, M. et al. Going nano: a new step toward understanding the processes governing freshwater ooid formation. *Geology* https://doi.org/10.1130/G32846.1 (2012).

73. Hoppe, P., Cohen, S. & Meibom, A. NanoSIMS: Technical aspects and applications in cosmochemistry and biological geochemistry. *Geostand. Geoanal. Res.* **37**, 111–154 (2013).

74. Perkins, A. M. Observations under electron microscopy of magnetic minerals extracted from speleothems. *Earth Planet. Sci. Lett.* **139**, 281–289 (1996).

75. Rasband, W. National Institutes of Health (NIH) of the United States of America. ImageJ – image processing and analysis in Java. https://imagej.nih.gov/ij (2020).

76. OpenMIMS from the National Resource for Imaging Mass Spectrometry (NRIMS). An ImageJ plugin for MIMS image analysis. https://github.com/BWHCNI/OpenMIMS (2020).

77. GeoMapApp from the Marine Geoscience Data System (MGDS) at Lamont-Doherty Earth Observatory of Columbia University. http://www.geomapapp.org (2020).

78. Ryan, W. B. F. et al. Global multi-resolution topography synthesis. *Geochem. Geophys. Geosyst.* **10**, Q03014 (2009).

Acknowledgements

Author contributions

Funding

Competing interests

The authors declare no competing interests.

Additional information

Supplementary information The online version contains supplementary material available at https://doi.org/10.1038/s43247-022-00358-0.

Correspondence and requests for materials should be addressed to Björn Klaes.

Peer review information *Communications Earth & Environment* thanks Victoria Smith, Silvia Frisia, and the other anonymous reviewer(s) for their contribution to the peer review of this work. Primary handling editor: Joe Aslin. Peer reviewer reports are available.

Reprints and permission information is available at http://www.nature.com/reprints

Publisher's note Springer Nature remains neutral with regard to jurisdictional claims in published maps and institutional affiliations.